

Deep-learning-based continuous attacks on QKD protocols

Théo Lejeune and François Damanet

Institut de Physique Nucléaire, Atomique et de Spectroscopie, CESAM, Université de Liège, 4000 Liège, Belgium

(Dated: Monday 7th October, 2024)

The most important characteristic of a Quantum Key Distribution (QKD) protocol is its security against third-party attacks, and the potential countermeasures available. While new types of attacks are regularly developed in the literature, they rarely involve the use of weak continuous measurement. Here, we design a new attack scheme called *Deep-learning-based continuous attack* (DLCA) that exploits continuous measurement together with the powerful pattern recognition capacities of deep recurrent neural networks. We show that, when applied to the BB84 protocol, our attack can be difficult to notice while still allowing the spy to extract significant information about the states of the qubits sent in the quantum communication channel. Finally, we study how the spy can exploit quantum feedback to further cover their tracks. Our attack scheme, while still at the early stages of a toy model, constitutes a potential threat which is worthwhile to be investigated, also as it could be applied to different QKD protocols and generalized in many different ways.

I. INTRODUCTION

In the last decades, the demand for fast, secure, and reliable data connections has significantly increased. To meet this demand, it is essential to enhance the computational power of network systems through high-performance technologies. Quantum computing is one such technology, showing a clear potential to outperform current classical computing systems. Quantum computing-assisted communications have therefore been extensively studied and developed in recent years, and hold great promise for improving communications and security in today's networks [1, 2].

At the same time, quantum computing represents also a threat in terms of security, in particular related to some asymmetric cryptographic algorithms such as RSA (Rivest-Shamir-Adleman) [3], a public key cryptosystem still used in many secure data transmissions to this day. Indeed, standard encryption techniques such as RSA, while very powerful, could be broken through Shor's algorithm, a quantum algorithm factoring large integers exponentially faster than the best-known classical algorithms [4].

While current quantum computing technology is still far from being enough advanced to break RSA, this motivated the elaboration of new encryption techniques based on quantum mechanical properties. Quantum Key Distribution (QKD), which aim is to implement the exchange of a private key over a public insecure channel between two parties, is the most famous category of quantum cryptography protocols [5]. The first and most known QKD protocol is the BB84, proposed by Charles Bennett and Gilles Brassard in 1984 [6], and uses linearly polarized photons travelling in an optical fiber. Among others are the B92 that uses entangled particles [7], the Differential-phase-shift which does not require a basis selection [8] or the Decoy State protocol designed to overcome photon number splitting attacks [9].

One of the main motivations to look for quantum cryptography protocols over classical ones originates from the perturbative nature of measurement in quantum mechanics. Indeed, any spy acting on a communication channel will influence the states of the qubits used to store the private key bits traveling inside, because of the collapse of the wavefunction, which makes the spy more easily detectable than in classical

communication protocols. Amongst the most studied types of attacks are the *Intercept-and-Resend* type, *Photon Number Splitting* (PNS) [10] and *Trojan Horse* (also called Large Pulse attack) [11, 12]. New Intercept-and-Resend attacks have been developed recently, such as *Blinding* [13], *Time shift* [14, 15] or *Dead-time* [16]. While some attacks employ strategies to make the spy measurement effect less detectable [e.g., by thermally blinding Bob's detector [13] or by monitoring the electromagnetic emissions of a QKD emitter and using a deep convolutional neural network (*Deep-learning-based radio-frequency side-channel attack* [17])], several of these attacks include projective measurements that usually provoke a perturbation on the photon state. Hence, if the two parties, say Alice and Bob, do not deploy specific countermeasures against the attacks [18], they can usually find a way to decide or not on the presence of a spy on the quantum communication channel, as studied in the past, although not extensively [19–22]. In this respect, a typical measure Alice and Bob can calculate (by sacrificing a few bits of the private key by sharing their measurement results on a public channel) is the Quantum Bit Error Rate (QBER), which is defined as the rate of incorrect results Bob gets when measuring the qubits sent by Alice in the right basis [23], i.e.,

$$\text{QBER} = \frac{N_{\text{error}}}{N_{\text{total}}}, \quad (1)$$

where N_{total} is the total number of qubits received where Bob used the right measurement basis, and N_{error} is the number of incorrect results he gets among these qubits. In the case of a perfect quantum communication channel, the QBER should be zero. However, in the presence of a spy, the qubits states are usually altered and the QBER non-zero despite Alice and Bob use the same basis for the qubits, which should thus signal the two parties that something went wrong. Complications then arise because in practice, the quantum channel is not perfectly isolated from its environment (the optical fiber could be leaky [24–26]) and the measurement apparatus of Bob could be defective, which contribute to another cause of QBER enhancement. Hence, distinguishing an attack from an intrinsic noise in the channel is not always easy.

In this paper, we develop a new type of attack based on continuous (homodyne) measurement [27] of individual po-

larized photons and apply it for concreteness in the context of the BB84 protocol. The general motivation beyond this is to evaluate the performance of attacks that produce only a small perturbation to the qubits, by contrast with the effects of projective measurement usually involved in the other types of attacks. In particular, we investigate how the effects of the spy measurement can be optimally hidden by the intrinsic noise of the quantum communication channel by minimizing the increase of the QBER due to the measurement. In the same time, we study how to maximize the information gain by the spy by feeding the outcome of the continuous measurement, also called homodyne photocurrents, to a Long Short-Term Memory (LSTM) recurrent neural network [28] to retrieve the initial states of the photons sent by Alice, which compose the private key generated.

This paper is organized as follows: In Sec. II we first remind the BB84 protocol step by step, present our model of the qubit dynamics in the quantum communication channel when subject to intrinsic dissipation and continuous measurement, investigate how a spy could use the outcome of this measurement to obtain the initial state of the qubit and present the neural network we implemented to do so. In Sec. III we compare the results obtained via a basic projective measurement (Intercept-and-Resend attack) and our measurement scheme. We then extend the theory to include quantum feedback, to try to decrease the measurement impact while keeping the same extracted information. Finally, in Sec. IV, we conclude and discuss potential perspectives.

II. MODEL AND METHODS

In this section, we first remind how the standard BB84 protocol works briefly, before presenting how we model the dynamics of the qubits used in the protocol when they are subjected to dissipation and continuous measurement in the quantum communication channel. Then, we describe the neural network that we envision a spy could use to retrieve the states of the qubits based on the continuous measurement they performed in the channel. Finally, we present how we quantify the impact of the measurement on the security of the protocol.

A. BB84 protocol

The BB84 protocol, sketched in Fig. 1, implements a shared secret key between two parties by storing private key bits in linearly polarized states of photons. There are four initial states: vertically and horizontally polarized states represented by $|0\rangle$ and $|1\rangle$ respectively, and two diagonally polarized states defined as

$$\begin{aligned} |+\rangle &= \frac{|0\rangle + |1\rangle}{\sqrt{2}}, \\ |-\rangle &= \frac{|0\rangle - |1\rangle}{\sqrt{2}}. \end{aligned} \quad (2)$$

These states define the Pauli-Z eigenbasis $\{|0\rangle, |1\rangle\}$ and the Pauli-X eigenbasis $\{|+\rangle, |-\rangle\}$ [29]. The protocol can then be

summarized as follows (see Fig. 1) [30]:

- Step 1: Alice chooses a random data bit string b (e.g., $b = 01011 \dots$). She encodes each data bit randomly as the quantum states $|0\rangle$ or $|+\rangle$ if the corresponding bit of b is 1 and $|1\rangle$ or $|-\rangle$ if the corresponding bit of b is 0.
- Step 2: Alice sends the resulting qubits to Bob via an optical fiber.
- Step 3: Bob receives the qubits and measures each of them in the Pauli-X or Pauli-Z eigenbasis at random.
- Step 4: Via the public channel Alice and Bob compare, for each qubit, the basis chosen by Alice to encode it and the basis chosen by Bob to measure this same qubit. They discard all the qubits where the two bases do not correspond.
- Step 5: Alice selects a subset of her bits to check on the interference caused by the spy – the so-called Eve –, and tells Bob which bits she chose. They both announce and compare the values of the check bits via the public channel and calculate the QBER given by Eq. (1). If it is higher than a threshold, they abort the protocol.

To increase the security of the protocol, two additional steps could be performed: information reconciliation (i.e., correcting bits that have been modified by dissipation [30, 31]), or privacy amplification (i.e., passing the generated key in a hash function to decrease Eve mutual information [30, 32, 33]), but which are not the purpose of this paper.

B. Dissipative qubit dynamics conditioned on measurement

For concreteness, we model the dynamics of each individual qubit in the quantum communication channel as subjected to i) intrinsic dissipation acting on the channel and ii) a continuous measurement performed by a spy (see Fig. 1). More specifically, we consider the following stochastic master equation (written here in Itô form)

$$\begin{aligned} d\rho_J &= -i[H, \rho_J] dt + \gamma_D \mathcal{D}[d]\rho_J dt \\ &+ \gamma_E \mathcal{D}[e]\rho_J dt + \sqrt{\gamma_E \eta} dW \mathcal{H}[e]\rho_J, \end{aligned} \quad (3)$$

where H is the channel Hamiltonian defined as $H = \omega \sigma_z$ for the initial states $|0\rangle$ or $|1\rangle$ and $H = \omega \sigma_x$ for $|+\rangle$ or $|-\rangle$ [24] with $\sigma_x = |0\rangle\langle 1| + |1\rangle\langle 0|$ and $\sigma_z = |0\rangle\langle 0| - |1\rangle\langle 1|$ the standard Pauli operators, where ρ_J is the density operator of the qubit conditioned on the measurement with efficiency $\eta \in [0, 1]$ of the homodyne current

$$J dt = \sqrt{\gamma_E} \langle e + e^\dagger \rangle dt + \frac{dW}{\sqrt{\eta}}, \quad (4)$$

and the superoperators $\mathcal{D}[o]$ and $\mathcal{H}[o]$ are defined as

$$\mathcal{D}[o] \cdot = o \cdot o^\dagger - \frac{1}{2}(o^\dagger o \cdot + \cdot o^\dagger o) \quad (5)$$

$$\mathcal{H}[o] \cdot = o \cdot + \cdot o^\dagger - \text{Tr}[o \cdot + \cdot o^\dagger] \cdot, \quad (6)$$

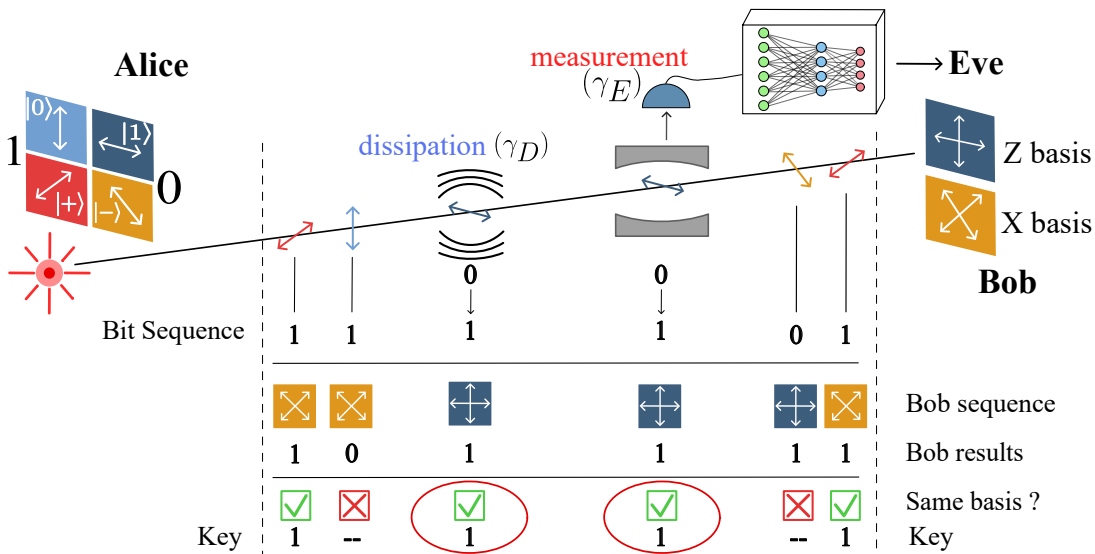


FIG. 1: Sketch representation of the attack scheme we develop in this paper applied on the BB84 protocol. Alice (A) sends linearly polarized photons to Bob (B) via an optical fiber, while travelling they are subject to dissipation with a rate γ_D and to weak measurement with a rate γ_E , as could be done e.g. via monitoring of a field coupled to the photon states of the optical fiber. The output of this measurement is treated using a neural network to determine the initial state. In the sketched example, Alice sends six photons to Bob, among which three are polarized in the Pauli-X eigenbasis and three in the Pauli-Z eigenbasis. Bob measures randomly in one of these two bases each of the photons received, and the basis chosen is the right one for four of these. However, even if the measurement basis is right, the two results circled in red are wrong due to dissipation and measurement that changed the qubit state in the optical fiber. In this example, if Alice and Bob compare all the measurements when they chose the same basis, the QBER [Eq. (1)] would be 50%.

for a given operator o . In Eq. (3), the first line represents the effect of the unitary dynamics of the channel governed by the Hamiltonian H as well as the effect of the intrinsic dissipation produced by the operator d occurring at rate γ_D , while the second line represents the effect of the eavesdropping produced by the operator e at rate γ_e , which decomposes into an incoherent term and a non-linear stochastic term, where dW is a Wiener increment satisfying $dW^2 = dt$. For concreteness, we set throughout this work the dissipation operator to be

$$d = \sigma_x, \quad (7)$$

to model the dissipation as a bit-flip error, but any other choice could be made without any additional complexity, depending e.g. on the specific optical fiber open system model investigated.

The measured current (4) allows in principle the spy to estimate the state of the qubit from the expectation value of $\langle e + e^\dagger \rangle$, as explained in the next section. The goal of the spy consists in i) minimizing the impact of their measurement on the quantum channel and ii) retrieving at best the initial qubit state sent by Alice.

C. Standard quantum state tomography

Since the spy wants to obtain the initial state of the photons from a continuous measurement, the data he has access to is the homodyne photocurrent of each photon he measured. Since the initial state is random, the spy cannot estimate the state

from averaging over many photocurrents: they have to estimate it from a single photocurrent for each qubit. In this scenario, using standard quantum state tomography (QST), which is the process of reconstructing the quantum state of a system from repeated measurements of a set of observables, is very difficult.

In [34], D'Ariano and Yuen reviewed a variety of concrete measurement schemes [35–39], and concluded that it is practically impossible to determine the wave function of a system from a single copy of it. More recent works on tomography, including plain averaging or maximum likelihood methods [40], direct inversion, distance minimization, maximum likelihood estimate with radial priors and Bayesian mean estimate [41], or Bayesian Homodyne and Heterodyne tomography [42], also show that it is difficult to reconstruct efficiently the initial state from one copy of the system or one measurement. In fact, without the measurement of a complete set of observables (a quorum), there is not enough information for the reconstruction as different states may give the exact same statistics on an incomplete set of observables [43, 44]. Hence, it is inefficient to use standard quantum state tomography techniques to estimate a qubit state from a single homodyne measurement on a photon, which motivated us to employ a deep learning approach, as explained below.

D. Neural network quantum tomography based on the measurement

The homodyne photocurrents resulting from the measurement are time series, and we therefore use a Long Short-Term Memory (LSTM) neural network, which is a type of Recurrent Neural Network (RNN) [28, 45]. RNNs consist of a unit cell that is repeated at every new input of the time-series data $\mathbf{x}^{(t)}$, producing an output $\mathbf{h}^{(t+1)}$ known as the hidden state. This hidden state is then combined with the next time-series input $\mathbf{x}^{(t+1)}$, allowing information to propagate through the sequence and have an impact on the outputs at future times (i.e., acting as a memory) [45]. LSTMs, in addition to a hidden state, use a cell state $\mathbf{c}^{(t)}$ to retain values for arbitrarily long periods of time [28]. Indeed, the units of a LSTM are composed of three gates (see Fig. 2): an input gate, an output gate, and a forget gate, to determine which information from the prior hidden state must be taken into account, stored and erased respectively. Therefore, this architecture is specifically designed to deal with long-time dependencies in sequential data. The architecture of the model we implemented is illustrated in Fig. 2. The input layer of our network is a LSTM one with 40 units in its hidden state, to take as input the time series data that are the photocurrents. We then use two dense hidden layers of 40 and 20 neurons, with activation functions set to ReLU and sigmoid respectively. The output layer is a 4 neurons softmax layer. The loss function we use for training is the sparse categorical cross entropy since we deal with a 4-class classification problem, and the optimizer is Adam with default parameters. The training consists in one epoch over 9×10^4 photocurrents while the testing is done on 10^4 photocurrents. Before entering the network the currents are standardized and flipped along their time axis.

Hence, our model takes as input the homodyne photocurrents the spy obtains while monitoring the photons, and outputs a probability distribution over the four possible initial states of the BB84 protocol (i.e., $|0\rangle$, $|1\rangle$, $|+\rangle$, $|-\rangle$). This supposes that the spy has the ability to train the neural network beforehand, using a similar photon source, optical fiber and detector than Alice and Bob, which is not unrealistic since one could assume the spy could know which kind of QKD devices Alice and Bob bought on the available market.

E. Impact of measurement VS Information gain

As explained earlier, the goal of the spy is to minimize their impact on the photon states while maximizing their information gain about the initial state sent by Alice. To quantify the impact of the measurement, we use the QBER introduced earlier [Eq. (1)], as it is directly measurable by Alice and Bob and allow them to assess the security of the protocol. To quantify the success of the spy in retrieving the initial state of the photons, we use the spy accuracy that we will denote by A . In the context of our deep learning approach, this is the neural network test accuracy [45] which is defined as the percentage of good predictions among all the predictions of the network on the

test set. However, when dealing with a projective measurement, this accuracy is defined as the probability that the spy measures the right state, as elaborated on below.

III. RESULTS

In this section, we study the impact of our attack and the information gained by the spy in different cases, from the analysis of the QBER and the accuracy A . We first compute the QBER in the case of no attack. Then, we study a simple standard projective measurement attack, before investigating our continuous measurement scheme. Finally, we close the section by studying the performance of a quantum feedback based on the measurement the spy could use to cover their tracks.

A. No attack

In the case where no spying is done on the quantum channel, which means there is no measurement and only the intrinsic dissipation, the QBER can easily be obtained from Eq. (3) with $e = 0$, which corresponds to a Lindblad master equation (see Appendix A), and reads

$$\text{QBER} = \frac{1}{4} - \frac{e^{-2\gamma_D t_f}}{4}, \quad 0 \leq \text{QBER} \leq 25\%, \quad (8)$$

where t_f is the total travel time of the qubit in the noisy quantum channel. Hence, the QBER ranges from 0 for a perfect channel to 25% for a very noisy channel or a very long travel time. This result is displayed as the black dashed line in Fig 3.

B. Attack via projective measurement

Let us now consider that the spy performs a projective measurement on the qubit at a certain time t^* ($0 < t^* < t_f$), as in an Intercept-and-Resend attack. Like Bob, the spy does not know in advance which measurement basis he should use, and thus measures randomly in the Pauli-X or Pauli-Z bases.

In this case, the information gain by the spy, or equivalently the accuracy A , can be calculated exactly by solving the Lindblad master equation with a single jump operator $L = \sigma_x$ (see Appendix B) and reads

$$A = \frac{5}{8} + \frac{e^{-2\gamma_D t^*}}{8}, \quad 62.5\% \leq A \leq 75\% \quad (9)$$

which depends on the time t^* at which the projective measurement is performed. Therefore, Eve must measure the photons as close to Alice as possible in order to maximize Eq. (9) and get as much information as possible on the private key, which is here bounded by 75%, meaning that the spy has at best 75% chance to guess the initial state sent by Alice.

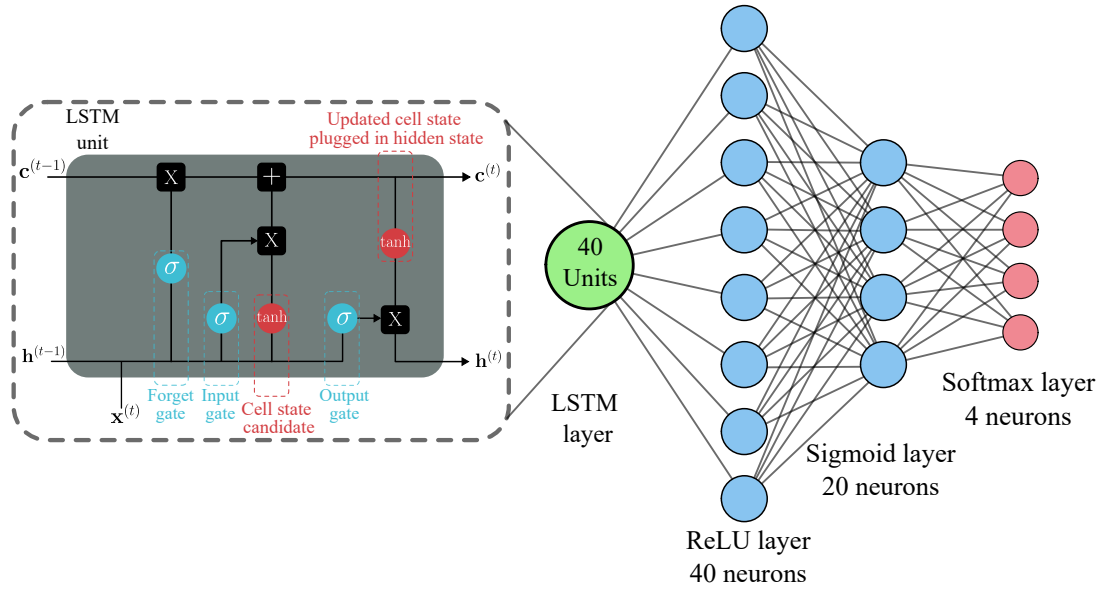


FIG. 2: Sketch representation of the LSTM architecture used in this paper. The input layer is composed of 40 LSTM units, and is followed by two dense hidden layers of 40 ReLU neurons and 20 sigmoid neurons respectively. The output layer is composed of 4 softmax neurons. On the left is a representation of one LSTM recurrent unit, composed of three gates with sigmoid activation functions (forget, input and output). These 3 gates determine which information from the prior hidden state must be erased, taken into account and stored respectively.

The QBER can also be obtained easily (see Appendix C), and reads

$$\text{QBER} = \frac{3}{8} - \frac{e^{-2\gamma_D t_f}}{8}, \quad 25\% \leq \text{QBER} \leq 37.5\%, \quad (10)$$

Interestingly, we see that the time t^* at which Eve performs her measurement does not impact the probability that Bob measures the state he is supposed to. Also, comparing Eqs. (8) and (10), we clearly see that Alice and Bob will always be able to distinguish the presence of the spy from intrinsic dissipation. This result is displayed as the dotted black line in Fig 3.

C. Attack via continuous measurement

We now discuss our new kind of attacks, based on an homodyne measurement of the photon that is fed to a LSTM neural network. When modelling the dynamics of photons under homodyne detection, one must set the measurement operator e of Eq. (3). First, let us use

$$e = \sigma_z, \quad (11)$$

and consider in the first instance that the homodyne measurement is performed during the whole travel time, set to $\gamma_D t_f = 3$, and with other parameters $\eta = 0.5$, $\omega = \gamma_E = \gamma_D$. With these parameters we get, from the solutions of Eq. (3), a QBER of 49% (red line in Fig 3), much higher than the 37% of the projective measurement obtained from Eq. (10) and the 24.4% of the case with dissipation only, obtained from Eq. (8). In addition, we get a neural network test accuracy $A \approx 71\%$, which is within the interval given by Eq. (9). We interpret this

result as coming from the fact that the states $|0\rangle$ and $|1\rangle$ being eigenstates of the measurement operator $e = \sigma_z$, the neural network can approximately distinguish these two while it must do random guess on the other two states ($|+\rangle$ and $|-\rangle$), which would lead to a test accuracy around 75% (see Appendix D). This suggests that the neural network puts a heavy weight on the early-time behavior of the photocurrent, as confirmed in Appendix E. Hence, we see that the spying accuracy achieved via this simple continuous measurement scheme is comparable with the one achieved via the projective measurement, but the QBER is higher.

In an attempt to reduce the impact of the spy while increasing its effectiveness, we now parameterize the measurement operator e as depending on an angle θ as

$$e = \cos(\theta)\sigma_x + \sin(\theta)\sigma_z, \quad (12)$$

so that it corresponds to a superposition of the two polarization bases.

Let us first look at the neural network test accuracy A of this new measurement operator as a function of θ/π , which is depicted in Fig. 4, together with the associated standard deviation. There are four angles leading to an accuracy around 90%, as summarized in Table I, which is much higher than the 71% found earlier. Note that the four angles seem equivalent given their values and the standard deviations.

To obtain the impact of the measurement on the BB84 protocol itself we average the QBER over the four possible initial states, and evaluate it as a function of θ and $\gamma_D t$, as displayed in Fig. 5. One can see there is a trade-off between the amount of information we can extract and the perturbation that

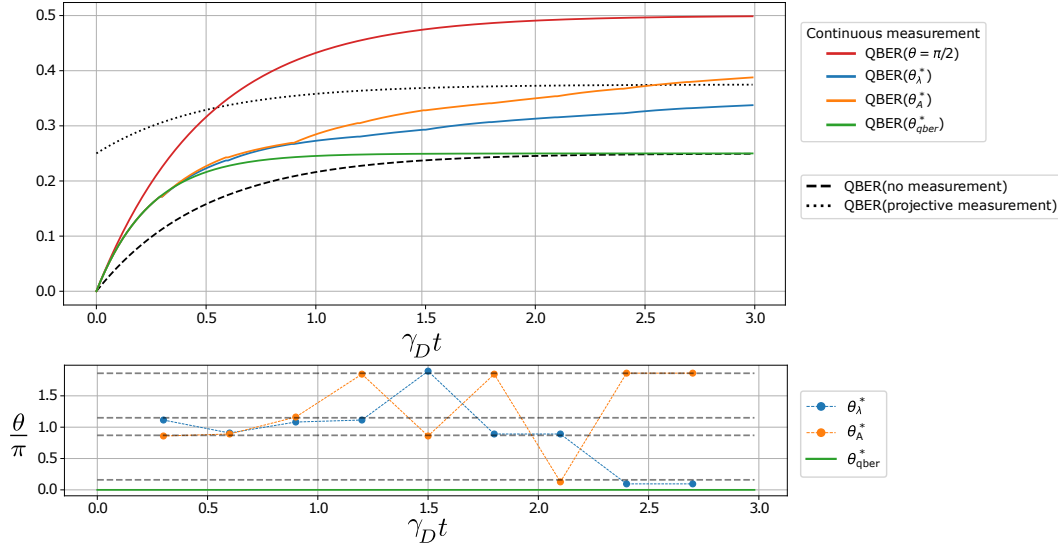


FIG. 3: Top: QBER as a function of $\gamma_D t$ for different attack schemes and angles θ . The black dashed line represents the QBER when no measurement is performed (i.e., produced only by intrinsic dissipation) [Eq. (8)]. The dotted black line is the QBER with dissipation and projective measurement [Eq. (10)] and the red line is the QBER caused by a continuous measurement with $e = \sigma_z$ ($\theta = \pi/2$). The orange line is the QBER when using the angle θ_A^* maximizing the accuracy (which we update every $\gamma_D t = 0.3$), the green line for the angle θ_{qber}^* minimizing the QBER, and the blue line for the angle θ_λ^* minimizing λ . Bottom: optimized angles with respect to the QBER itself (green line), the NN test accuracy (orange line) and λ (blue line).

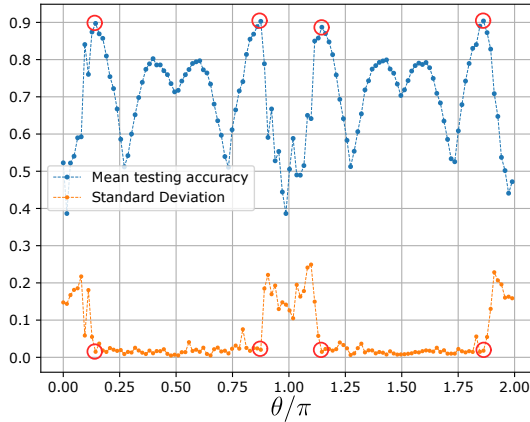


FIG. 4: Mean estimated accuracy A (blue) and standard deviation (orange) of the model on the test set as a function of θ . The photocurrents of the test set were obtained using Eq. (3) and (4). Circled in red are the four maximum accuracy values and their corresponding standard deviations, reported in Table I. Other parameters are $\gamma_D t_f = 3$ and $\omega = \gamma_E = \gamma_D$.

this measurement induces. Indeed, the angles that minimize the QBER, which are $\theta = 0 \pm k\pi$, $k \in \mathbb{Z}$, yield a low test accuracy, thus decreasing the information the spy obtains (see Fig. 4). In order to quantify this tradeoff, we define a new quantity $\lambda(\theta)$ as the QBER divided by the accuracy A of the network for a

θ	mean accuracy	standard deviation
0.16π	89.8%	1.6%
0.87π	90.3%	2.1%
1.15π	88.7%	1.5%
1.86π	90.4%	1.8%

TABLE I: Mean accuracy A of the neural network and corresponding standard deviations for the optimal values of θ found in Fig. 4.

given measurement basis (i.e., a given θ)

$$\lambda(\theta) = \frac{\text{QBER}(\theta)}{A(\theta)}, \quad (13)$$

which is shown for $\gamma_D t_f = 3$ in Fig. 6. We see that among the four measurement angles maximizing the spy accuracy (circled in red), $\theta = 1.86\pi$ yields the lowest λ ratio, with an accuracy around 90% and a QBER around 37%, though the other angles give similar performances.

The top panel of Fig. 3 gathers all the QBER discussed above. In addition, three other lines are present: the QBER for a continuous measurement when θ is set to minimize the QBER itself (green line), to maximize the accuracy (orange line), and finally to minimize λ (blue line). In the bottom panel, the θ values of these three lines are represented, along with the four optimal angles from Table I as guides to the eye (black dashed lines). The QBER optimized with respect to itself is at first higher than the one from no measurement at all, before converging to the same value of 25%. However, even

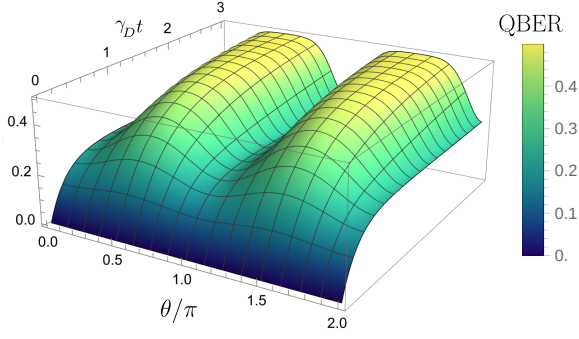


FIG. 5: QBER as a function of time and measurement angle θ . The evolution of the photon states through time was obtained using Eq. (3). Other parameters are $\gamma_D t_f = 3$ and $\omega = \gamma_E = \gamma_D$.

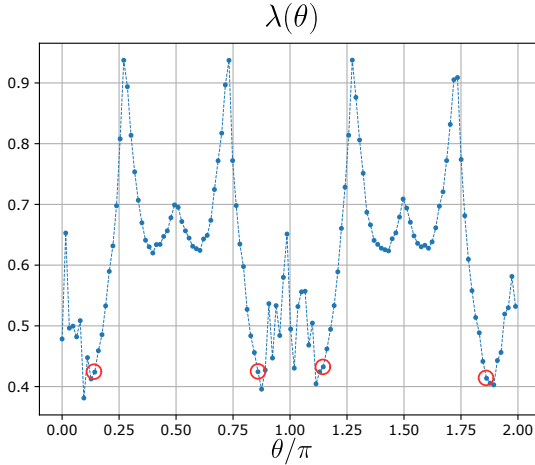


FIG. 6: $\lambda(\theta)$ [Eq. (13)] as a function of θ . Circled in red are the four values of θ maximizing A found in Fig. 4 and reported in Table I. Other parameters are $\gamma_D t_f = 3$ and $\omega = \gamma_E = \gamma_D$.

though Alice and Bob could never detect this eavesdropping (at least for large $\gamma_D t_f$), the neural network manages to learn something from it since its mean accuracy for this case ($\theta = 0$, i.e., $e = \sigma_x$) is higher than 25% (see Fig. 4). Also, the measurement optimized with respect to the accuracy yields a lower QBER than a projective measurement for $\gamma_D t_f \leq 2.5$ and the one optimized with respect to λ yields an even lower QBER, but still higher than the green line.

Finally, to make the measurement more realistic, one can reduce the duration of the continuous measurement so that it starts later than the initial time and finishes before the final time. We choose here the optimal measurement angle found earlier, $\theta = 1.86\pi$, and set it to start at $\gamma_D t = 0.1$ and define a duration Δt of the continuous measurement with the aim of decreasing its impact on the qubit states while keeping a reasonable neural network test accuracy. As shown in Fig. 7, which displays A as a function of $\gamma_D \Delta t$, the accuracy reaches 86.1% with a reasonable standard deviation (2%) when measuring between

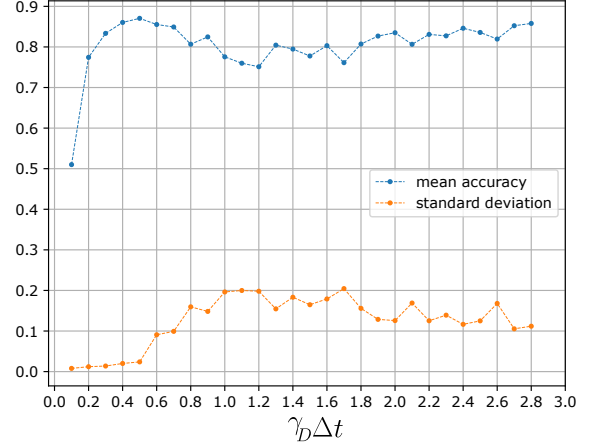


FIG. 7: Mean accuracy A and standard deviation of the neural network as a function of the measurement length $\gamma_D \Delta t$. The photocurrents were obtained using Eq. (3) and (4). Other parameters are $\gamma_D t_f = 3$ and $\omega = \gamma_E = \gamma_D$.

$\gamma_D t = 0.1$ and 0.5 . For longer duration, we see that the accuracy is reasonable but the standard deviation becomes very high as compared to Fig. 4. This suggests that the initial time-evolution (i.e., before $\gamma_D t = 0.1$), which is not fed to the neural network here, is crucial to make it sharp. Altogether, taking $\theta = 1.86\pi$ and the optimal duration $\gamma_D \Delta t = 0.4$, we obtain an accuracy of 86.1% and a QBER of 27.6%, this latter representing only a 2.6% increase compared to the time-evolved state where no measurement is made. Comparatively, the *Time shift* [14, 15] attack scheme yields an accuracy around 60 – 70% and an increase of the QBER between 1 and 2%. Hence, though the noise model for the fiber is not the same, our new attack scheme seems to provide similar QBER increases and very high accuracies, which suggests it is a potential threat that should be investigated further. A summary of the results of this section can be found in Table II.

D. Attack via continuous measurement and quantum feedback

As a final section, we briefly investigate here the possibility for the spy to apply quantum feedback based on their measurement [27] with the aim of covering their track. We thus adapt Eq. (3) to include the action of a feedback which yields [27]

$$\begin{aligned} d\rho_J = & \left\{ -i[H, \rho_J] + \gamma_E \mathcal{D}[e]\rho_J - i\gamma_E [f, e\rho_J + \rho_J e^\dagger] \right\} dt \\ & + \gamma_E \mathcal{D}[f]\rho_J \frac{dt}{\eta} + \gamma_E dW \mathcal{H} [\sqrt{\eta}e - if/\sqrt{\eta}] \rho_J \\ & + \gamma_D \mathcal{D}[d]\rho_J dt, \end{aligned} \quad (14)$$

where f is the feedback operator. The non-selective evolution equation of the system can be obtained by taking the ensemble average of this equation, which removes the term containing dW . By doing so we obtain the homodyne mediated feedback

master equation in the Lindblad form [46]:

$$\begin{aligned} \dot{\rho}_J = & -i[H + \frac{\gamma_E}{2}(e^\dagger f + f e), \rho_J] + \gamma_D \mathcal{D}[d]\rho_J \\ & + \gamma_E \mathcal{D}[e - if]\rho_J + \frac{1-\eta}{\eta} \gamma_E \mathcal{D}[f]\rho_J. \end{aligned} \quad (15)$$

The effect of feedback is to replace the e operator by $e - if$, to add an extra term to the Hamiltonian and a term vanishing for the efficiency $\eta = 1$.

To find the optimal feedback operator we parameterize f as

$$f = \cos(\phi)\sigma_x + \sin(\phi)\sigma_z. \quad (16)$$

We also set the measurement and the feedback to be performed between $\gamma_D t = 0.1$ and 0.5 (the optimal duration found in the previous section). The QBER as a function of the measurement angle θ and the feedback angle ϕ is displayed in Fig. 8 for $\gamma_D t_f = 3$. For the optimal measurement angle $\theta = 1.86\pi$ found earlier, the feedback angle minimizing the QBER of Fig. 8 is $\phi = 0.94\pi$. With that angle, we obtain a QBER of 29.9%, which is greater than without feedback, which could be due to the fact that an unconditional feedback introduces more noise in the system than it prevents. From this analysis, it seems that quantum feedback does not lead to any improvement of the attack, but many other parameter regimes and feedback schemes, such as feedback conditioned on the measurement record, could be explored in the future.

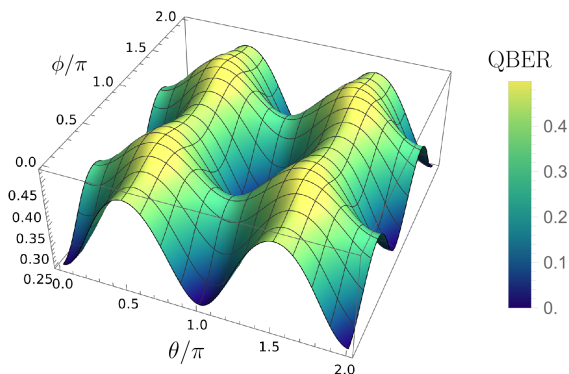


FIG. 8: QBER(θ, ϕ) as a function of the measurement and feedback angles: θ and ϕ . The evolution of the photon states was obtained using Eq. (15). Other parameters are $\gamma_D t_f = 3$ and $\omega = \gamma_E = \gamma_D$.

IV. CONCLUSION

In this paper, we introduced a new type of attack on QKD protocols based on continuous measurement that, used as an input of a trained recurrent neural network, allows the spy to retrieve with high accuracy the initial states sent by one of the

parties without being significantly noticed. We denote our attack as a *Deep-learning-based continuous attack* (DLCA). Although more quantitative and comparison analyses should be done, also in terms of noise models considered for the optical fiber, our attack scheme exhibits performances similar to other attacks, which makes it a potential serious threat worthy to be explored in future works.

To go further, one could use a more complex and realistic noise model of the optical fiber. In [24], Kozubov *et al.* span the space using three states: the vacuum state and the states we denoted $|0\rangle$ and $|1\rangle$ in this work (i.e., horizontally and vertically polarized photons). By doing so, they take into account the non-zero probability that the photon is absorbed in the optical fiber. They also tune the phenomenological parameters involved in the master equation, which allows to take into account the phenomena of birefringence, isotropic absorption, and dichroism. However, the depolarizing quantum channel [30] is a commonly used noise model and would be worth considering in our study. In addition, one could consider the potential losses caused by the imperfection of Alice and Bob detectors.

In addition, one could investigate practical implementations of our attack scheme involving homodyne detection of single photon [48], by exploiting evanescent waves in optical fibers [49] or quantum memories [50].

The next step could also be to determine the possible countermeasures one could implement to make the BB84 protocol robust against our attack, such as decoy states protocols [9, 51]. However, one could also investigate how our scheme could be applied to coherent states continuous variable protocols [52, 53] exploiting homodyne or heterodyne detection, or entanglement-based protocols such as the E91 [54], the BBM92 [55] or on device-independent protocols [56, 57]. Entanglement-based protocols are promising for satellites QKD, which is currently being extensively studied by the scientific community [58–61]. One could thus explore the generalization of our attack and its practical implementation to satellite QKD.

Also, we considered here the introduction of unconditional quantum feedback. However, one could consider feedback conditioned on the measurement outcome history and thus implement conditional feedback, yielding Non-Markovian dynamics. Also, one could describe the dynamics of the monitored system (without feedback) with a Non-Markovian approach, using for example the cHEOM method [62].

Finally, one could also analyze our attack in the context of QKD protocols using qudits, also called high dimensional quantum key distributions (HDQKD) [63–65].

ACKNOWLEDGMENTS

We thank Jérôme Denis and John Martin for helpful initial discussions on the topic.

Dissipation	Attack	Impact (QBER)	Information gain (Accuracy)
$d = 0$	$e = 0$	0.0	0.0
$d = \sigma_x$	$e = 0$	25%	0.0
$d = \sigma_x$	Projective measurement	37.5%	69.4%
$d = \sigma_x$	Continuous measurement	49%	72%
$d = \sigma_x$	$e = \sigma_z$	27.6%	86.1%
$d = \sigma_x$	$e = 0.90\sigma_x - 0.43\sigma_z$ ($\theta = 1.86\pi$)	(2.6% increase)	
	Time Shift	1 – 2% increase	60 – 70%

TABLE II: Summary of the QBER and accuracies A generated by the different attack schemes we analyzed. We compare our results with the Time-Shift attack [15, 47], even though the noise model we use is different. The parameters are $\gamma_D t_f = 3$, $\gamma_D \Delta t = 0.4$, $\gamma_D t^* = 0.3$ and $\omega = \gamma_E = \gamma_D$. We set Eve measurement time $\gamma_D t^*$ to 0.3 such that it corresponds to the middle of the optimized continuous measurement.

Appendix A: Analytical derivation of the QBER without attacks

Without measurement, we model the evolution of a photon state in the optical fiber with the Lindblad master equation

$$\dot{\rho} = -i[H, \rho] + \gamma_D \left(L\rho L^\dagger - \frac{1}{2}L^\dagger L\rho - \frac{1}{2}\rho L^\dagger L \right), \quad (\text{A1})$$

where the jump operator $L = \sigma_x$ models bit flip errors, and the Hamiltonian is $H = \omega\sigma_z$ for the initial states $|0\rangle$ and $|1\rangle$ and $H = \omega\sigma_x$ for the initial states $|+\rangle$ and $|-\rangle$. We denote the matrix elements of ρ in the basis $\{|0\rangle, |1\rangle\}$ as $\rho_{ij} = \text{Tr}(|j\rangle\langle i|\rho) = \langle i|\rho|j\rangle$ ($i, j = 0, 1$). Projecting the

master equation in the computational basis gives the following linear set of equations for the density matrix elements

$$\begin{cases} \dot{\rho}_{00} = \gamma_D(\rho_{11}(t) - \rho_{00}(t)) \\ \dot{\rho}_{01} = \gamma_D(\rho_{10}(t) - \rho_{01}(t)) \\ \dot{\rho}_{10} = \gamma_D(\rho_{01}(t) - \rho_{10}(t)) \\ \dot{\rho}_{11} = \gamma_D(\rho_{00}(t) - \rho_{11}(t)) \end{cases} \quad (\text{A2})$$

which is independent of the Hamiltonian term of the master equation for both cases $H = \omega\sigma_x$ and $H = \omega\sigma_z$. Resolving this system gives:

$$\rho(t) = \begin{pmatrix} \frac{e^{-2\gamma_D t}}{2}(1 + e^{2\gamma_D t})\rho_{00}(0) + \frac{e^{-2\gamma_D t}}{2}(-1 + e^{2\gamma_D t})\rho_{11}(0) & \frac{e^{-2\gamma_D t}}{2}(1 + e^{2\gamma_D t})\rho_{01}(0) + \frac{e^{-2\gamma_D t}}{2}(-1 + e^{2\gamma_D t})\rho_{10}(0) \\ \frac{e^{-2\gamma_D t}}{2}(-1 + e^{2\gamma_D t})\rho_{01}(0) + \frac{e^{-2\gamma_D t}}{2}(1 + e^{2\gamma_D t})\rho_{10}(0) & \frac{e^{-2\gamma_D t}}{2}(-1 + e^{2\gamma_D t})\rho_{00}(0) + \frac{e^{-2\gamma_D t}}{2}(1 + e^{2\gamma_D t})\rho_{11}(0) \end{pmatrix} \quad (\text{A3})$$

which describes the state of the qubit in the channel at time t .

There are four possible states for Alice to send: $\{|0\rangle, |1\rangle, |+\rangle, |-\rangle\}$.

In the case $\rho(0) = |0\rangle\langle 0|$, Eq. (A3) gives

$$\rho(t) = \begin{pmatrix} \frac{e^{-2\gamma_D t}}{2} + \frac{1}{2} & 0 \\ 0 & -\frac{e^{-2\gamma_D t}}{2} + \frac{1}{2} \end{pmatrix} \quad (\text{A4})$$

so that the probability that the qubit is in the state $|0\rangle$ after going through the optical fiber is $\rho_{00}(t) = \frac{e^{-2\gamma_D t}}{2} + \frac{1}{2}$.

In the case $\rho(0) = |1\rangle\langle 1|$, we find

$$\rho(t) = \begin{pmatrix} -\frac{e^{-2\gamma_D t}}{2} + \frac{1}{2} & 0 \\ 0 & \frac{e^{-2\gamma_D t}}{2} + \frac{1}{2} \end{pmatrix} \quad (\text{A5})$$

and the probability that the qubit is in the state $|1\rangle$ is given by $\rho_{11}(t) = \frac{e^{-2\gamma_D t}}{2} + \frac{1}{2}$.

In the case $\rho(0) = |+\rangle\langle +|$, we find

$$\rho(t) = \begin{pmatrix} \frac{1}{2} & \frac{1}{2} \\ \frac{1}{2} & \frac{1}{2} \end{pmatrix}. \quad (\text{A6})$$

Finally, in the case $\rho(0) = |-\rangle\langle -|$, we find

$$\rho(t) = \begin{pmatrix} \frac{1}{2} & -\frac{1}{2} \\ -\frac{1}{2} & \frac{1}{2} \end{pmatrix}. \quad (\text{A7})$$

As the states $|+\rangle$ and $|-\rangle$ are eigenstates of the σ_x jump operator, they will not change when traveling through the optical fiber: they are insensitive to the dissipation process. These states are decoherence-free states (or dark states) for the given master equation.

When the photon reaches Bob at time t_f , he chooses randomly one of the two available bases (i.e., Pauli-X and Pauli-Z). The probabilities above correspond to Bob measuring in the right

basis. On the other hand, the probability that Alice sends one of the four states is $\frac{1}{4}$ because she chooses randomly the polarization basis and the state in this polarization. Thus, the probability \mathbb{P}_b (same results) that Bob gets the right state is

$$\begin{aligned} \mathbb{P}_b(\text{same results}) &= \frac{1}{4} \frac{1}{2} \left(\frac{e^{-2\gamma_D t_f}}{2} + \frac{1}{2} \right) + \frac{1}{4} \frac{1}{2} \left(\frac{e^{-2\gamma_D t_f}}{2} + \frac{1}{2} \right) \\ &\quad + \frac{1}{4} \frac{1}{2} \cdot 1 + \frac{1}{4} \frac{1}{2} \cdot 1 \\ &= \frac{e^{-2\gamma_D t_f}}{4} + \frac{3}{4}. \end{aligned} \quad (\text{A8})$$

Since it corresponds to one minus the QBER, we finally have

$$\text{QBER} = \frac{1}{4} - \frac{e^{-2\gamma_D t_f}}{4}, \quad (\text{A9})$$

which corresponds to Eq. (8) in the main text.

Appendix B: Analytical derivation of Eve accuracy for a projective measurement

The result above allows us to easily determine Eve accuracy in the case she performs a projective measurement at time t^* . Indeed, when the photon reaches Eve at time t^* , she also chooses randomly one of the two available bases. The probabilities above correspond to someone measuring in the right basis. However, if Eve does not, her probability of detecting the right state is still $1/2$ as she can random guess. Thus, the probability that Eve deduces the right state (i.e., the accuracy A) can be obtained from Eq. (A8), which yields

$$\begin{aligned} A &= \frac{1}{4} \frac{1}{2} \left(\frac{e^{-2\gamma_D t^*}}{2} + \frac{1}{2} + \frac{1}{2} \right) + \frac{1}{4} \frac{1}{2} \left(\frac{e^{-2\gamma_D t^*}}{2} + \frac{1}{2} + \frac{1}{2} \right) \\ &\quad + \frac{1}{4} \frac{1}{2} \left(1 + \frac{1}{2} \right) + \frac{1}{4} \frac{1}{2} \left(1 + \frac{1}{2} \right) \\ &= \frac{e^{-2\gamma_D t^*}}{8} + \frac{5}{8}, \end{aligned} \quad (\text{B1})$$

which corresponds to Eq. (9) in the main text.

Appendix C: Analytical derivation of Bob accuracy for a projective measurement (intercept-and-resend attack)

After Eve's projective measurement at time t^* , the photon is in the state she measured, and thus evolves according to Eq. (A3) until it reaches Bob at time t_f . To simplify the process, we will look in detail to the case where Alice sends the initial state $|0\rangle$ which generalizes easily to the other states. Since we want to obtain the probability that Bob measures the state Alice sent, which is $1 - \text{QBER}$, and since they will both, at some part of the protocol, compare the bases they respectively used and discard the differing ones (see Sec. II A), we consider that Bob measures in the Pauli-Z basis $\{|0\rangle, |1\rangle\}$. There are four distinct cases, each corresponding to a different measurement result for Eve.

If she measures in the Pauli-Z basis (probability $1/2$) and she measures the state $|0\rangle$ [probability $(1 + e^{-2\gamma_D t^*})/2$], the photon will be in the state $|0\rangle$ right after. Thus Bob will measure the state $|0\rangle$ with probability $(1 + e^{-2\gamma_D(t_f - t^*)})/2$.

However, if Eve measures in the Pauli-Z basis but the result is $|1\rangle$ [probability $(1 - e^{-2\gamma_D t^*})/2$] then the probability that Bob measures the state $|0\rangle$ is $(1 - e^{-2\gamma_D(t_f - t^*)})/2$.

If Eve measures in the Pauli-X basis (probability $1/2$), the result will be either $|+\rangle$ or $|-\rangle$, each with probability $1/2$, which is the state that will reach Bob since they are not affected by the dissipation. Therefore, Bob's result will be $|0\rangle$ or $|1\rangle$, each with probability $1/2$.

Altogether, this yields the probability that Bob measures the state $|0\rangle$ if Alice sent it

$$\begin{aligned} \mathbb{P}_b(|0\rangle) &= \frac{1}{2} \left(\frac{1}{2} + \frac{e^{-2\gamma_D t^*}}{2} \right) \left(\frac{1}{2} + \frac{e^{-2\gamma_D(t_f - t^*)}}{2} \right) \\ &\quad + \frac{1}{2} \left(\frac{1}{2} - \frac{e^{-2\gamma_D t^*}}{2} \right) \left(\frac{1}{2} - \frac{e^{-2\gamma_D(t_f - t^*)}}{2} \right) \\ &\quad + 2 \times \frac{1}{2} \times \frac{1}{2} \times \frac{1}{2} \\ &= \frac{2}{4} + \frac{e^{-2\gamma_D t_f}}{4}. \end{aligned} \quad (\text{C1})$$

Following the same procedure for the three other initial states, we obtain

$$\mathbb{P}_b(|1\rangle) = \frac{2}{4} + \frac{e^{-2\gamma_D t_f}}{4}, \quad (\text{C2})$$

$$\begin{aligned} \mathbb{P}_b(|+\rangle) &= \mathbb{P}_b(|-\rangle) = \frac{1}{2} \times 1 \times 1 + 2 \times \frac{1}{2} \times \frac{1}{2} \times \frac{1}{2} \\ &= \frac{3}{4}. \end{aligned} \quad (\text{C3})$$

Since Alice sends each of these states with equal probability, the final probability is

$$\begin{aligned} \mathbb{P}_b(\text{right result}) &= \frac{1}{4} \mathbb{P}_b(|0\rangle) + \frac{1}{4} \mathbb{P}_b(|1\rangle) \\ &\quad + \frac{1}{4} \mathbb{P}_b(|+\rangle) + \frac{1}{4} \mathbb{P}_b(|-\rangle) \\ &= \frac{5}{8} + \frac{e^{-2\gamma_D t_f}}{8}. \end{aligned} \quad (\text{C4})$$

Since it corresponds to one minus the QBER, we finally have

$$\text{QBER} = \frac{3}{8} - \frac{e^{-2\gamma_D t_f}}{8}, \quad (\text{C5})$$

which corresponds to Eq. (10) in the main text.

Appendix D: Confidence of the model for σ_z and σ_x measurements

We compute the confidence of our model by summing the probability that the network outputs for the ground truth state (i.e., the initial state it must predict). The results are displayed in Fig. 9(a) and 9(b) for the measurement operators $e = \sigma_z$

and $e = \sigma_x$ respectively. For σ_z , the network is correct almost every time for the states $|0\rangle$ and $|1\rangle$ while for the two others it either only predicts $|+\rangle$ or $|-\rangle$ depending on the first it has seen during training, which varies since the batches order is random. However, these four trainings yield similar accuracies. This result confirms our intuition that the model cannot distinguish the states $|+\rangle$ and $|-\rangle$ when setting the measurement operator to $e = \sigma_z$, thus performing random guess. On the other hand for σ_x , we see that the network much more often predicts one of the four states (the first it has seen during training) and almost never outputs one or several of them.

The architecture is robust to changes in the training order for the Pauli-Z measurement operator while it is not for the Pauli-X one, which is due to the fact that the mean accuracy achieved with the latter is low (50%) while the standard deviation is high (15%), meaning that the network has trouble learning

something meaningful from the dataset and is thus unstable.

Appendix E: LSTM hidden states activation through time

For the initial state $|0\rangle$ (Fig. 10a), some hidden states of the LSTM network activate at the early times of the time-series before maintaining a non-zero activity during the whole time sequence. However, for the initial state $|+\rangle$ (Fig. 10b), the hidden states retain their activity until the end of the time series, which could indicate that more information about the initial state is contained in the later times of the photocurrents. The early activation of the hidden states in both cases demonstrates that most information is contained in the first time steps of the currents, and is memorized by the hidden units until the output.

-
- [1] P. Botsinis, D. Alanis, Z. Babar, H. V. Nguyen, D. Chandra, S. X. Ng, and L. Hanzo, *IEEE Communications Surveys & Tutorials* **21**, 1209 (2019).
- [2] O. D. Okey, S. S. Maidin, R. Lopes Rosa, W. T. Toor, D. Carrillo Melgarejo, L. Wuttisittikulij, M. Saadi, and D. Zegarra Rodríguez, *Sustainability* **14**, 10.3390/su142315901 (2022).
- [3] R. L. Rivest, A. Shamir, and L. Adleman, *Commun. ACM* **21**, 120–126 (1978).
- [4] P. W. Shor, *SIAM Journal on Computing* **26**, 1484–1509 (1997).
- [5] R. Renner, *Security of Quantum Key Distribution*, Ph.D. thesis, ETH Zurich (2006).
- [6] C. H. Bennett and G. Brassard, *Theoretical Computer Science* **560**, 7 (2014), theoretical Aspects of Quantum Cryptography – celebrating 30 years of BB84.
- [7] C. H. Bennett, *Phys. Rev. Lett.* **68**, 3121 (1992).
- [8] K. Inoue, E. Waks, and Y. Yamamoto, *Phys. Rev. Lett.* **89**, 037902 (2002).
- [9] W.-Y. Hwang, *Physical Review Letters* **91**, 10.1103/physrevlett.91.057901 (2003).
- [10] G. Brassard, N. Lütkenhaus, T. Mor, and B. C. Sanders, *Phys. Rev. Lett.* **85**, 1330 (2000).
- [11] N. Gisin, S. Fasel, B. Kraus, H. Zbinden, and G. Ribordy, *Phys. Rev. A* **73**, 022320 (2006).
- [12] V. M. Artem Vakhitov and D. R. Hjelme, *Journal of Modern Optics* **48**, 2023 (2001), <https://www.tandfonline.com/doi/pdf/10.1080/09500340108240904>.
- [13] L. Lydersen, C. Wiechers, C. Wittmann, D. Elser, J. Skaar, and V. Makarov, *Opt. Express* **18**, 27938 (2010).
- [14] V. Makarov, A. Anisimov, and J. Skaar, *Phys. Rev. A* **74**, 022313 (2006).
- [15] Y. Zhao, C.-H. F. Fung, B. Qi, C. Chen, and H.-K. Lo, *Physical Review A* **78**, 10.1103/physreva.78.042333 (2008).
- [16] H. Weier, H. Krauss, M. Rau, M. Fürst, S. Nauerth, and H. Weinfurter, *New Journal of Physics* **13**, 073024 (2011).
- [17] A. Baliuka, M. Stöcker, M. Auer, P. Freiwang, H. Weinfurter, and L. Knips, *Physical Review Applied* **20**, 10.1103/physrevapplied.20.054040 (2023).
- [18] A. R. Dixon, J. F. Dynes, M. Lucamarini, B. Fröhlich, A. W. Sharpe, A. Plews, W. Tam, Z. L. Yuan, Y. Tanizawa, H. Sato, S. Kawamura, M. Fujiwara, M. Sasaki, and A. J. Shields, *Scientific Reports* **7**, 1978 (2017).
- [19] T. Metger and R. Renner, *Nature Communications* **14**, 10.1038/s41467-023-40920-8 (2023).
- [20] R. Kumar, F. Mazzoncini, H. Qin, and R. Alléaume, *Scientific Reports* **11** (2021).
- [21] S. R. M and C. M. B, *Comprehensive analysis of bb84, a quantum key distribution protocol* (2023), arXiv:2312.05609 [quant-ph].
- [22] A. Adu-Kyere, E. Nigussie, and J. Isoaho, *Sensors* **22**, 10.3390/s22166284 (2022).
- [23] V. Scarani, H. Bechmann-Pasquinucci, N. J. Cerf, M. Dušek, N. Lütkenhaus, and M. Peev, *Rev. Mod. Phys.* **81**, 1301 (2009).
- [24] A. Kozubov, A. Gaidash, and G. Miroshnichenko, *Phys. Rev. A* **99**, 053842 (2019).
- [25] G. P. Miroshnichenko, *Optics and Spectroscopy* **112**, 777 (2012).
- [26] G. P. Miroshnichenko and A. A. Sotnikova, *Optics and Spectroscopy* **112**, 327 (2012).
- [27] H. M. Wiseman and G. J. Milburn, *Quantum Measurement and Control* (Cambridge University Press, 2009).
- [28] S. Hochreiter and J. Schmidhuber, *Neural Computation* **9**, 1735 (1997).
- [29] N. D. Mermin, *Quantum Computer Science: An Introduction* (Cambridge University Press, 2007).
- [30] M. A. Nielsen and I. L. Chuang, *Quantum Computation and Quantum Information: 10th Anniversary Edition* (Cambridge University Press, 2010).
- [31] D. Elkouss, J. Martinez-Mateo, and V. Martin, *Information reconciliation for quantum key distribution* (2011), arXiv:1007.1616 [quant-ph].
- [32] Y.-G. Yang, P. Xu, R. Yang, Y.-H. Zhou, and W.-M. Shi, *Scientific Reports* **6**, 19788 (2016).
- [33] B. Yan, Q. Li, H. Mao, and N. Chen, *Quantum Information Processing* **21**, 130 (2022).
- [34] G. M. D’Ariano and H. P. Yuen, *Phys. Rev. Lett.* **76**, 2832 (1996).
- [35] O. Alter and Y. Yamamoto, *Phys. Rev. Lett.* **74**, 4106 (1995).
- [36] Y. Aharonov, J. Anandan, and L. Vaidman, *Phys. Rev. A* **47**, 4616 (1993).
- [37] M. Ueda and M. Kitagawa, *Phys. Rev. Lett.* **68**, 3424 (1992).
- [38] A. Imamoglu, *Phys. Rev. A* **47**, R4577 (1993).
- [39] A. Royer, *Phys. Rev. Lett.* **73**, 913 (1994).
- [40] N. Cerf, G. Leuchs, and E. Polzik, *Quantum Information With Continuous Variables of Atoms and Light* (2007).
- [41] R. Schmied, *Journal of Modern Optics* **63**, 1744–1758 (2016).

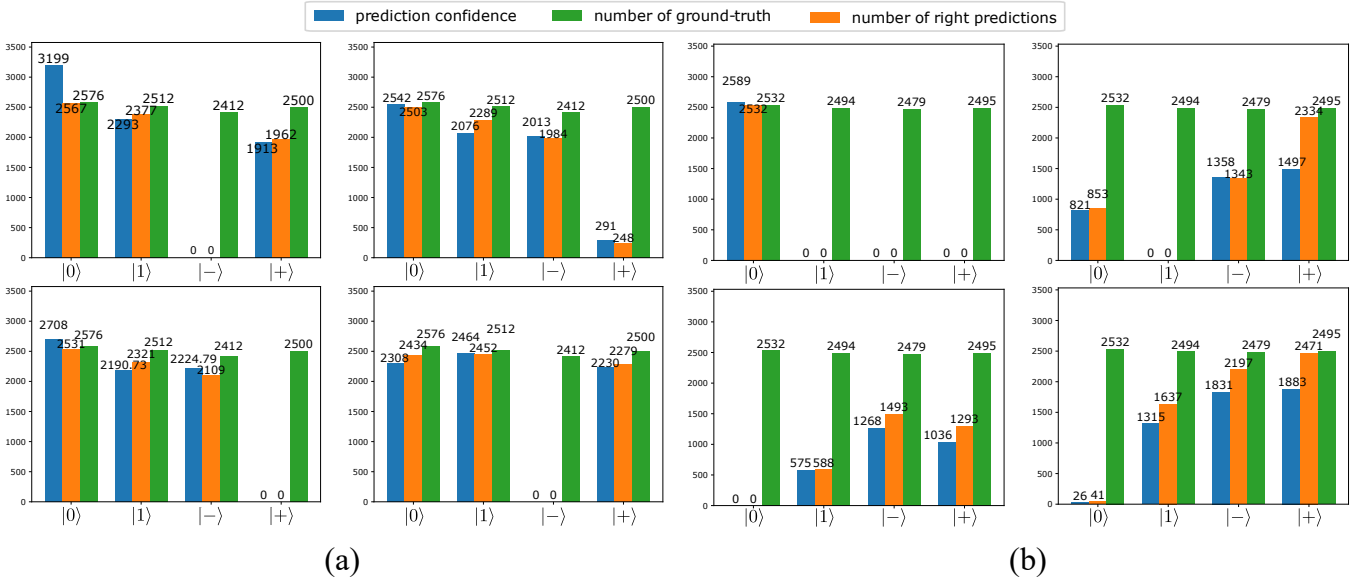


FIG. 9: Comparison of the number of right predictions, ground truth and of the model confidence about them for each initial states, for four different training. These results are obtained from a measurement performed with the operator (a) $e = \sigma_z$ and (b) $e = \sigma_x$. In panel (a), the network is correct almost every time for the states $|0\rangle$ and $|1\rangle$ while for the two others it either only predicts $|+\rangle$ or $|-\rangle$ depending on the first it has seen during training (order of the batches is random). These four trainings yielded accuracies around 71%. In panel (b), we see that the network much more often predicts one of the four states (the first it has seen during training) and almost never outputs one or several of them. The four trainings yielded accuracies of 25%, 34%, 45% and 63% respectively (going from left to right and top to bottom).

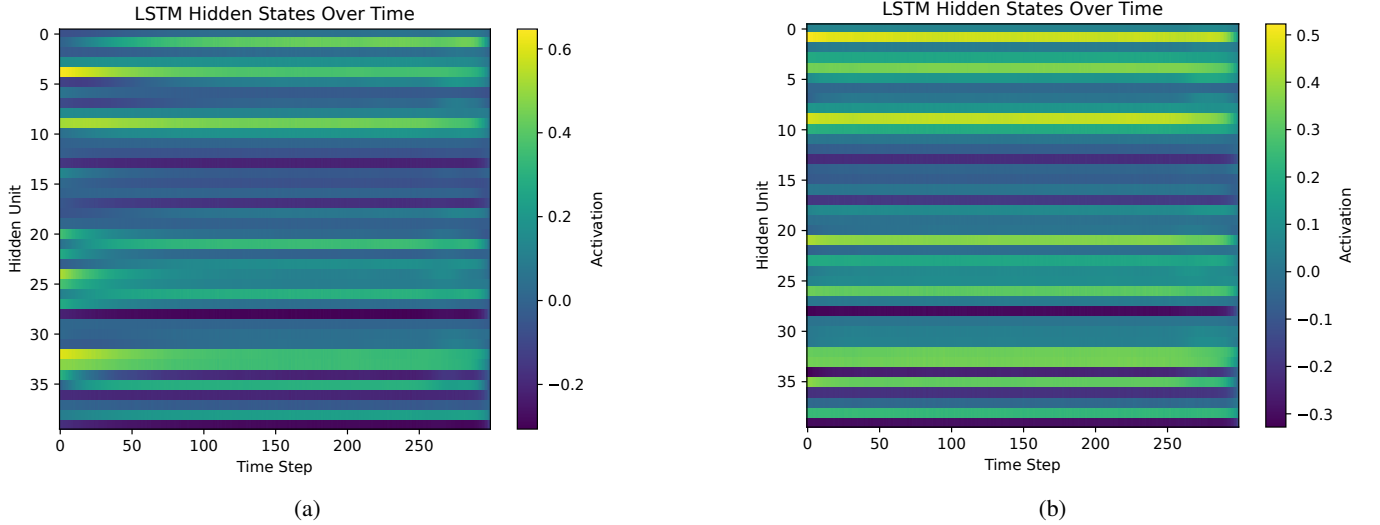


FIG. 10: LSTM hidden states activations through the input time steps for the initial state $|0\rangle$ [panel (a)] and $|+\rangle$ [panel (b)].

[42] J. C. Chapman, J. M. Lukens, B. Qi, R. C. Pooser, and N. A. Peters, *Optics Express* **30**, 15184 (2022).
 [43] N. Mosco and L. Maccone, *Physics Letters A* **449**, 128339 (2022).
 [44] J. Altepeter, E. Jeffrey, and P. Kwiat (Academic Press, 2005) pp. 105–159.
 [45] I. Goodfellow, Y. Bengio, and A. Courville, *Deep Learning* (MIT Press, 2016).
 [46] H. M. Wiseman, *Phys. Rev. A* **49**, 2133 (1994).

[47] B. Qi, C.-H. F. Fung, H.-K. Lo, and X. Ma, Time-shift attack in practical quantum cryptosystems (2006), arXiv:quant-ph/0512080 [quant-ph].
 [48] A. I. Lvovsky and M. G. Raymer, *Reviews of Modern Physics* **81**, 299–332 (2009).
 [49] M. Bertolotti, C. Siglia, and A. Guzman, Evanescent waves in optical waveguides, in *Evanescent Waves in Optics: An Introduction to Plasmonics* (Springer International Publishing, Cham, 2017) pp. 69–110.

- [50] A. I. Lvovsky, B. C. Sanders, and W. Tittel, *Nature Photonics* **3**, 706 (2009).
- [51] H.-K. Lo, X. Ma, and K. Chen, *Phys. Rev. Lett.* **94**, 230504 (2005).
- [52] Y. Zhang, Y. Bian, Z. Li, S. Yu, and H. Guo, *Applied Physics Reviews* **11**, 10.1063/5.0179566 (2024).
- [53] N. Jain, H.-M. Chin, H. Mani, C. Lupo, D. S. Nikolich, A. Kordts, S. Pirandola, T. B. Pedersen, M. Kolb, B. Ömer, C. Pacher, T. Gehring, and U. L. Andersen, *Nature Communications* **13**, 4740 (2022).
- [54] A. K. Ekert, *Phys. Rev. Lett.* **67**, 661 (1991).
- [55] C. H. Bennett, *Phys. Rev. Lett.* **68**, 3121 (1992).
- [56] A. Acín, N. Brunner, N. Gisin, S. Massar, S. Pironio, and V. Scarani, *Phys. Rev. Lett.* **98**, 230501 (2007).
- [57] W. Zhang, T. van Leent, K. Redeker, R. Garthoff, R. Schwonnek, F. Fertig, S. Eppelt, W. Rosenfeld, V. Scarani, C. C.-W. Lim, and H. Weinfurter, *Nature* **607**, 687 (2022).
- [58] S.-K. Liao, W.-Q. Cai, W.-Y. Liu, L. Zhang, Y. Li, J.-G. Ren, J. Yin, Q. Shen, Y. Cao, Z.-P. Li, F.-Z. Li, X.-W. Chen, L.-H. Sun, J.-J. Jia, J.-C. Wu, X.-J. Jiang, J.-F. Wang, Y.-M. Huang, Q. Wang, Y.-L. Zhou, L. Deng, T. Xi, L. Ma, T. Hu, Q. Zhang, Y.-A. Chen, N.-L. Liu, X.-B. Wang, Z.-C. Zhu, C.-Y. Lu, R. Shu, C.-Z. Peng, J.-Y. Wang, and J.-W. Pan, *Nature* **549**, 43 (2017).
- [59] S. Ecker, J. Pseiner, J. Piris, and M. Bohmann, *Advances in entanglement-based qkd for space applications* (2022), arXiv:2210.02229 [quant-ph].
- [60] J. Yin, Y. Cao, Y.-H. Li, S.-K. Liao, L. Zhang, J.-G. Ren, W.-Q. Cai, W.-Y. Liu, B. Li, H. Dai, G.-B. Li, Q.-M. Lu, Y.-H. Gong, Y. Xu, S.-L. Li, F.-Z. Li, Y.-Y. Yin, Z.-Q. Jiang, M. Li, J.-J. Jia, G. Ren, D. He, Y.-L. Zhou, X.-X. Zhang, N. Wang, X. Chang, Z.-C. Zhu, N.-L. Liu, Y.-A. Chen, C.-Y. Lu, R. Shu, C.-Z. Peng, J.-Y. Wang, and J.-W. Pan, *Science* **356**, 1140 (2017), <https://www.science.org/doi/pdf/10.1126/science.aan3211>.
- [61] Y.-A. Chen, Q. Zhang, T.-Y. Chen, W.-Q. Cai, S.-K. Liao, J. Zhang, K. Chen, J. Yin, J.-G. Ren, Z. Chen, S.-L. Han, Q. Yu, K. Liang, F. Zhou, X. Yuan, M.-S. Zhao, T.-Y. Wang, X. Jiang, L. Zhang, W.-Y. Liu, Y. Li, Q. Shen, Y. Cao, C.-Y. Lu, R. Shu, J.-Y. Wang, L. Li, N.-L. Liu, F. Xu, X.-B. Wang, C.-Z. Peng, and J.-W. Pan, *Nature* **589**, 214 (2021).
- [62] V. Link, K. Müller, R. G. Lena, K. Luoma, F. m. c. Damant, W. T. Strunz, and A. J. Daley, *PRX Quantum* **3**, 020348 (2022).
- [63] M. Zahidy, D. Ribezzo, C. D. Lazzari, I. Vagniluca, N. Biagi, R. Müller, T. Occhipinti, L. K. Oxenløwe, M. Galili, T. Hayashi, D. Cassioli, A. Mecozzi, C. Antonelli, A. Zavatta, and D. Bacco, *Nature Communications* **15**, 1651 (2024).
- [64] X.-Y. Yan, N.-R. Zhou, L.-H. Gong, Y.-Q. Wang, and X.-J. Wen, *Quantum Information Processing* **18**, 271 (2019).
- [65] D. Halevi, B. Lubotzky, K. Sulimany, E. G. Bowes, J. A. Hollingsworth, Y. Bromberg, and R. Rapaport, *High-dimensional quantum key distribution using orbital angular momentum of single photons from a colloidal quantum dot at room temperature* (2024), arXiv:2405.03377 [quant-ph].